Sensors & Actuators: B. Chemical 377 (2023) 133101

Contents lists available at ScienceDirect

Sensors and Actuators: B. Chemical

journal homepage: www.elsevier.com/locate/snb

Dual-strategy ECL biosensor based on rare Eu(II,III)-MOF as probe with antenna effect and sensitization for CYFRA 21-1 trace analysis

Lu Zhao [a], Beibei Wang [a], Chao Wang [b], Dawei Fan [a], Xuejing Liu [a], Qin Wei [a], Huangxian Ju [a], Dan Wu [a,*]

[a] Collaborative Innovation Centre for Green Chemical Manufacturing and Accurate Detection, School of Chemistry and Chemical Engineering, University of Jinan, Jinan 250022, Shandong, China

[b] Department of Rehabilitation, Shandong Provincial Hospital Affiliated to Shandong First Medical University, Jinan 250021, Shandong, China

ARTICLE INFO

Keywords:
Mixed-valence Eu-MOF
Antenna effect
Sensitization
CYFRA 21-1
Electrochemiluminescence biosensor

ABSTRACT

The choices of luminophore and coreactant accelerator are crucial in a constructed electrochemiluminescence (ECL) biosensor. In this work, a mixed-valence Eu-MOF ($Sr(HCOO)_2$:Eu^{2+}/Eu^{3+}) as luminophore was synthesized based on the precursor of eight-coordinated $Sr(HCOO)_2$ with $P4_12_12$ space group and tetragonal crystal structure. The doped Eu^{3+} was in-situ reduced to Eu^{2+} by efficient reductant combined with ligand 2-aminoterephthalic acid and solvent thermal decomposition product dimethylamine, then the Eu^{2+} substitutively coordinated Sr $(HCOO)_2$ due to the same ion radius and coordination environment between Eu^{2+} and Sr^{2+}. Through UV–vis, fluorescence spectra and density functional theory (DFT) calculations, the specific luminescence mechanisms of $Sr(HCOO)_2$:Eu^{2+}/Eu^{3+} with the antenna effect and sensitization were verified. Thanks to the strongest catalysis of Ag to $K_2S_2O_8$ and the high active sites, the AgCl rice roll-shaped nanoclusters (AgCl RRNCs) as coreactant accelerator encouraged the production of more $SO_4^{\bullet-}$. Thereout, the constructed ECL biosensor showed high performance in trace detection of cytokeratin 19 fragment 21-1 (CYFRA 21-1) with low limit of detection (2.73 fg/mL) and wide detection range (5 fg/mL ~ 100 ng/mL), which met the requirement for diagnosis and post-operative monitoring non-small-cell lung cancer in clinical treatment completely. These strategies also provided feasible ideas for efficient and stable other biosensors except ECL.

1. Introduction

Electrochemiluminescence (ECL) immunoassay offers a convenient way to quantitative determination for tumor markers in vivo accurately and sensitively and thus has been played an essential role in fundamental biological research and clinical diagnosis thanks to its low background, wide dynamic ranges and plain operation [1–4]. Nowadays, lanthanide metal-organic frameworks (Ln-MOFs) are a kind of ideal materials as ECL probes with merits of long luminescent lifetimes, strong antenna effect, ultrahigh surface area and active sites [5–8]. Among them, Eu-MOFs have possessed massive attention by virtue of their excellent luminescence characteristics. The europium ion among Eu-MOFs is usually presented as trivalent [9], but the mixed-valence Eu-MOFs (+2, +3) possess greater ECL luminescence performance, which is resulted from the superimposed effect or sensitization by different energy level structures corresponding to *f-f* transition of Eu^{3+} and *f-d* transition of Eu^{2+} [7]. The similar ion radius and configuration of extra-nuclear electron between Eu^{3+} and Eu^{2+} make sensitization of Eu^{2+} to Eu^{3+} easier by energy transfer from the higher energy level of Eu^{2+} to Eu^{3+} [7,10], which contributes to the higher ECL efficiency of the mixed-valence Eu-MOFs.

Nevertheless, the eminent bottleneck remain in the highly oxidizability of Eu^{2+} the resulting difficulties in preparation between the mixed-valence Eu-MOFs [9,11,12]. The common way of doping Eu^{2+} is to use sodium borohydride as a strong reducing agent or create a reducing atmosphere with the help of nitrogen and argon [11,12]. These means make the operating conditions harsh, dangerous and costly. A reported strategy is that Sr^{2+} and Eu^{2+} with the same ion radius can provide coordination sites with each other, which can realize the substitution coordination of Eu^{2+} to Sr^{2+} in Sr-MOF after the simple transformation from Eu^{3+} to Eu^{2+} using reductive organic substances as ligands and reaction solvents respectively [13]. This tactic provided us with an idea of simple synthesis of mixed-valence MOF under mild conditions.

* Corresponding author.
E-mail address: wudan791108@163.com (D. Wu).

https://doi.org/10.1016/j.snb.2022.133101
Received 8 September 2022; Received in revised form 2 November 2022; Accepted 30 November 2022
Available online 2 December 2022

Based on the sensitization of Eu^{2+} to Eu^{3+}, the Eu^{3+} in mixed-valence Eu-MOFs as dominating ECL center can emit strong signals in the co-reactant medium of $K_2S_2O_8$. To further improve the ECL performance of the system, a feasible method is to catalyze the decomposition of $K_2S_2O_8$ into $SO_4^{\bullet-}$ [6,7]. Ag(I) is superior to other metal catalysts (such as Co^{2+}, Ce^{3+}, Ni^{2+}) for $K_2S_2O_8$ activation [14], and Ag-based materials are a kind of good biological fixative via Ag-amino coordination bond [9], therefore Ag(I)-based catalysts are appropriate for the construction of ECL immunosensor particularly. In addition, compared with single structure, complicated structure catalysts (like core-shell and hollow structure) have ample catalytic active sites, high specific surface area and enhanced volume controllability [15,16]. These indicate that the Ag (I)-based catalysts with core-shell structure can be considered to play a significant role in enhancing the performance of ECL sensors.

In this work, an ultrasensitive ECL biosensor, constituted by a mixed-valence Eu-MOF ($Sr(HCOO)_2$:Eu^{2+}/Eu^{3+}) as ECL luminophore and a rice roll-shaped nanoclusters of AgCl nanoparticles (AgCl RRNCs) as co-reactant accelerator, was firstly constructed to fulfill the trace detection of cytokeratin 19 fragment 21-1 (CYFRA 21-1). CYFRA 21-1 is a fragment of cytokeratins19, and it can be can be considered as a representative biomarker for squamous cell carcinomas detection to achieve the diagnosis of lung cancer [17]. Here, the synthesis of $Sr(HCOO)_2$:Eu^{2+}/Eu^{3+} was depended on the precursor of eight-coordinated Sr $(HCOO)_2$ with $P4_12_12$ space group and tetragonal crystal structure. The doped Eu^{3+} was in-situ reduced to Eu^{2+} by ligand 2-aminoterephthalic acid and solvent thermal decomposition product dimethylamine subsequently, then the Eu^{2+} substitutively coordinated $Sr(HCOO)_2$ due to the same ion radius and coordination environment. Powered by the special structure, the $Sr(HCOO)_2$:Eu^{2+}/Eu^{3+} possessed the antenna effect and the sensitization, which endowing the $Sr(HCOO)_2$:Eu^{2+}/Eu^{3+} with efficient luminescence. In addition, the AgCl RRNCs provided abundant sites for immobilization of antibody and catalysis of $K_2S_2O_8$, thus enhancing the sensitivity of the biosensor further. Based on these, the ECL biosensor had low limit of detection (LOD) with 2.73 fg/mL for the detection of CYFRA 21-1. The ultrasensitive analysis of CYFRA 21-1 can provide a way to early diagnose and postoperatively monitor non-small-cell lung cancer in clinical treatment, especially squamous cell cancer [18,19].

2. Experimental section

2.1. Preparation of the $Sr(HCOO)_2$:Eu^{2+}/Eu^{3+}

$Sr(HCOO)_2$:Eu^{2+}/Eu^{3+} was synthesized according to the literature with some modifications [13], and the synthetic process was shown in Fig. 1 A. 0.1 mmol of 1,3,5-benzenetricarboxylic acid, 0.1 mmol of 2-aminoterephthalic acid, 0.8 mmol of $SrCl_2{\cdot}6\ H_2O$ and 0.1 mmol of Eu $(NO_3)_3{\cdot}6\ H_2O$ were dissolved in 5 mL of DMF. Next, 100 μL of 45% hydroiodic acid solution and 300 μL of ethanol were appended into the above mixture, and the mixed solution was reacted for 2 days at 120 °C

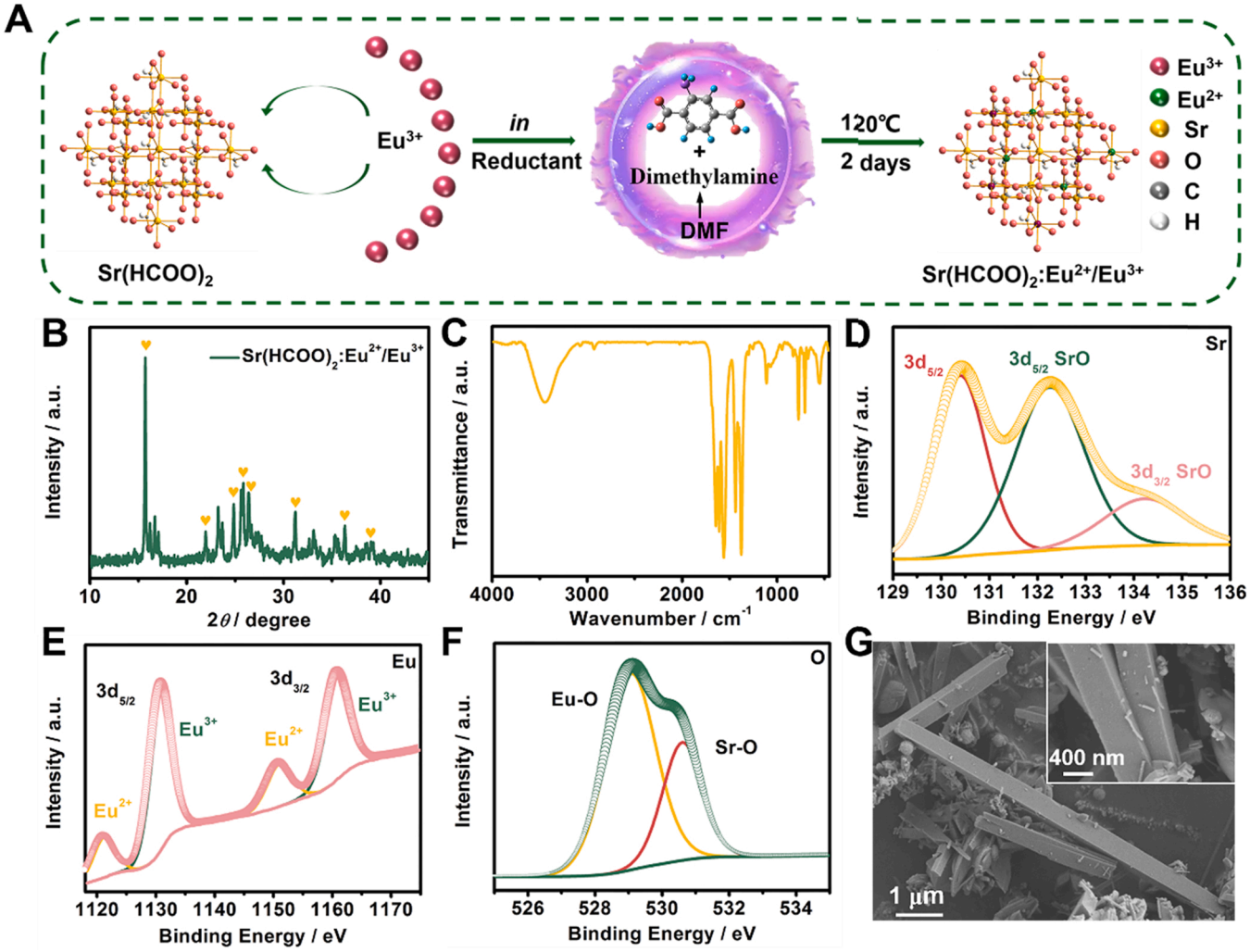

Fig. 1. (A) The synthesis route of $Sr(HCOO)_2$:Eu^{2+}/Eu^{3+}. (B) XRD pattern and (C) FT-IR spectrum of as-synthesized $Sr(HCOO)_2$:Eu^{2+}/Eu^{3+}. XPS spectra in the (D) Sr 3d, (E) Eu 3d and (F) O 1 s regions for $Sr(HCOO)_2$:Eu^{2+}/Eu^{3+}. (G) SEM images of $Sr(HCOO)_2$:Eu^{2+}/Eu^{3+}.

in an oil bath. The off-white powders were gained after washing and centrifugation three times via DMF and ethanol.

2.2. Preparation of the AgCl RRNCs

AgCl RRNCs were synthesized according to the literature with some modifications [20,21]. 54 mg of PVP (Mw: 55,000) and 45 mg of NaCl were added to 12 mL of heated ethylene glycol at 60 °C for 30 min. After dissolving, the 57 mg/mL of $AgNO_3$/ethylene glycol solution was added into the above solution and then heated at 60 °C for 30 min. The mixture was heated to 150 °C for 4 h. The reaction was shielded from light. The product was gained after washing and centrifugation three times via H_2O.

2.3. Construction procedures of the biosensor

The embellishment steps of electrode were displayed in Scheme 1. Firstly, 8 μL AgCl solution was fallen on the smoothed glassy carbon electrode (GCE). Then, 8 μL Ab_1 solution (100 μg/mL) was dropped on the AgCl stratum via Ag-NH_2 bonding. Next, 5 μL of bovine serum albumins (BSA) and 5 μL of different concentrations of antigen were dripped. Then the electrode was dried at 4 °C and washed with water to remove the unbonded parts upon dripping 5 μL of Ab_2 @$Sr(HCOO)_2$:Eu^{2+}/Eu^{3+} onto electrode. Finally, the constructed ECL biosensor was kept at 4 °C.

2.4. ECL detection of CYFRA 21-1

The ECL behavior was monitored over the optimized experiment conditions. The scan range was − 1.8–0 V. The concentrations of $K_2S_2O_8$, $Sr(HCOO)_2$:Eu^{2+}/Eu^{3+} and AgCl RRNCs were 80 mM, 6 mg/mL and 6 mg/mL. The pH value of phosphate buffered saline (PBS) was 7.4. The ECL tests were carried out at a photomultiplier tube voltage of 800 V and a scanning rate of 100 mV/s.

3. Result and discussion

3.1. Characterizations of $Sr(HCOO)_2$:Eu^{2+}/Eu^{3+}

The crystallographic structure of as-prepared $Sr(HCOO)_2$:Eu^{2+}/Eu^{3+} was determined by means of Xray diffraction (XRD) analysis (Fig. 1B). The diffraction peaks at 15.72°, 22.00°, 24.78°, 25.80°, 25.81°, 31.16°, 36.30° and 39.11° can correspond to the simulated peaks, which demonstrated the successful synthesis of the $Sr(HCOO)_2$:Eu^{2+}/Eu^{3+} [13]. Fig. 1 C showed the FTIR spectrum of $Sr(HCOO)_2$: Eu^{2+}/ Eu^{3+}, from which the structural characters and functional groups of it can be verified. The appearance of free -NH_2 groups in 2-aminoterephthalic acid ligand can be said by the vibration of the N-H bending mode at 771 cm^{-1} and the symmetric and asymmetric stretching of free -NH_2 at 3443 and 3242 cm^{-1} [22]. The characteristic bands at 1108, 708 and 552 cm^{-1} were corresponding to benzene rings [7]. The strong peaks at 1649, 1562 and 1435 cm^{-1} were ascribed to the asymmetric and symmetric stretching vibrations of the carboxylic groups, meanwhile the partial carboxyl that deprotonated and coordinated with Eu^{3+} were confirmed via the asymmetric stretching vibration $\nu_{as}(COO^-)$ (1602 cm^{-1}) and the symmetric stretching vibration $\nu_s(COO^-)$ (1375 cm^{-1}) [8,23]. The complete chemical compositions of Sr $(HCOO)_2$:Eu^{2+}/Eu^{3+} were revealed by the X-ray photoelectron spectroscopy (XPS) survey spectrum in Fig. S1. As can be seen in Fig. 1D, the high-resolution spectrum of Sr 3d was divided into two parts, in which the $3d_{5/2}$ orbit was the binding energies at 130.4 and 132.3 eV and the $3d_{3/2}$ orbit was the binding energy at 134.3 eV. The peaks at 132.3 eV and 134.3 eV were assigned to SrO, and the peak at 130.4 eV was attributed to the Sr from MOF lattice [24,25]. In Fig. 1E, the high resolution XPS spectrum of Eu 3d showed two valence states. The peaks of Eu^{2+} located at 1121.4 and 1151.2 eV respectively, which can be assigned to the $3d_{5/2}$ and $3d_{3/2}$. The peaks of Eu^{3+} located at 1131.2 and 1161.3 eV respectively, which can be assigned to the $3d_{5/2}$ and $3d_{3/2}$ [6]. In the high-resolution spectrum of O 1 s (Fig. 1 F), the two peaks, one belonged to Eu-O bonding (529.0 eV) and the other to Sr-O bonding (530.6 eV), indicating the substitution coordination of Eu in Sr-MOF [8, 26]. The morphology of the as-prepared $Sr(HCOO)_2$:Eu^{2+}/Eu^{3+} was presented cuboid nanorods with a uniform width of 500 nm in Fig. 1 G. The energy-dispersive spectrometry (EDS) results indicated the existence and uniform distribution of Eu, O, Sr elements (Fig. S2).

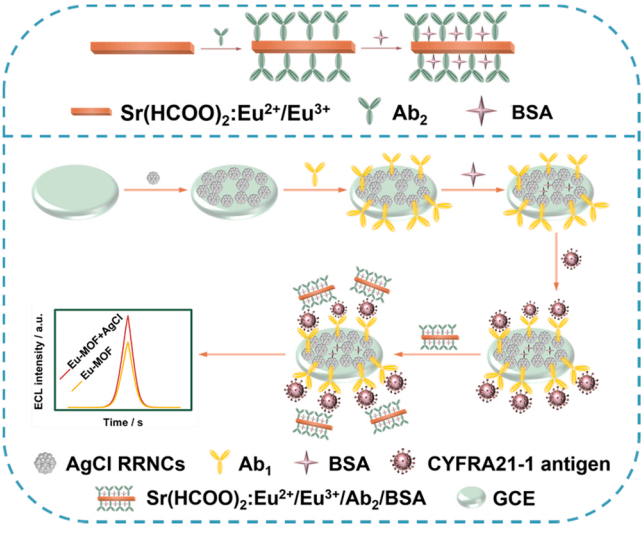

Scheme 1. The construction procedures and enhancement mechanism of the ECL biosensor.

3.2. Characterizations of AgCl RRNCs

As can be seen from Fig. 2 A, the XRD patterns confirmed the ingredient of AgCl RRNCs in the as-prepared coreactant accelerator. The different peaks at 27.8°, 32.2°, 46.2°, 54.8°, 57.5°, 67.5°, 74.5° and 76.7° were matched to the crystallographic planes of (111), (200), (220), (311), (222), (400), (331) and (420), which can correspond to the simulated pattern of AgCl (JCPDs 31-1328). The XPS survey spectrum of AgCl RRNCs was shown in Fig. S3. In the high-resolution Ag 3d spectrum (Fig. 2B), the two energy levels severally split into two peaks, the binding energies at 367.2 and 368.6 eV were assigned to Ag $3d_{5/2}$ of AgCl and elemental Ag, the binding energies at 373.1 and 374.2 eV were assigned to Ag $3d_{3/2}$ of AgCl and elemental Ag. From the XPS results of Cl 2p spectrum (Fig. 2 C), the high peaks at 195.0 and 196.5 eV were matched with Cl $2p_{3/2}$ and $2p_{1/2}$, respectively [27]. The SEM and TEM images were observed that the as-prepared AgCl depicted 70 nm uniform nanoparticles, the AgCl NPs agglomerated into a rice roll-shaped clusters morphology with about 650 nm diameter (Fig. 2D-F). The energy-dispersive X-ray spectroscopy (EDS) and mapping results clearly revealed that both the Cl and Ag elements distributed on AgCl RRNCs uniformly (Fig. S4).

3.3. The luminescence mechanism of $Sr(HCOO)_2$:Eu^{2+}/Eu^{3+}

Two important components make up the luminous mechanism of Sr $(HCOO)_2$:Eu^{2+}/Eu^{3+}: the antenna effect and the sensitization. Firstly, the UV–vis absorption spectrum of $Sr(HCOO)_2$:Eu^{2+}/Eu^{3+} was observed characteristic peaks of Eu^{2+} at 264 and 318 nm, which were attributed to $4f^7 \rightarrow 4f^6 5d^1$ transition (Fig. 3 A) [28]. Then in the fluorescence spectra of $Sr(HCOO)_2$:Eu^{2+}/Eu^{3+}, the found excitation peak at 354 nm belonged to the $4f^7 \rightarrow 4f^6 5d^1$ transition of Eu^{2+} [6]. The emission spectrum showed a broad band of Eu^{2+} and two sharp bands of Eu^{3+}. To be more specific, the broad band can be divided into two peaks centered

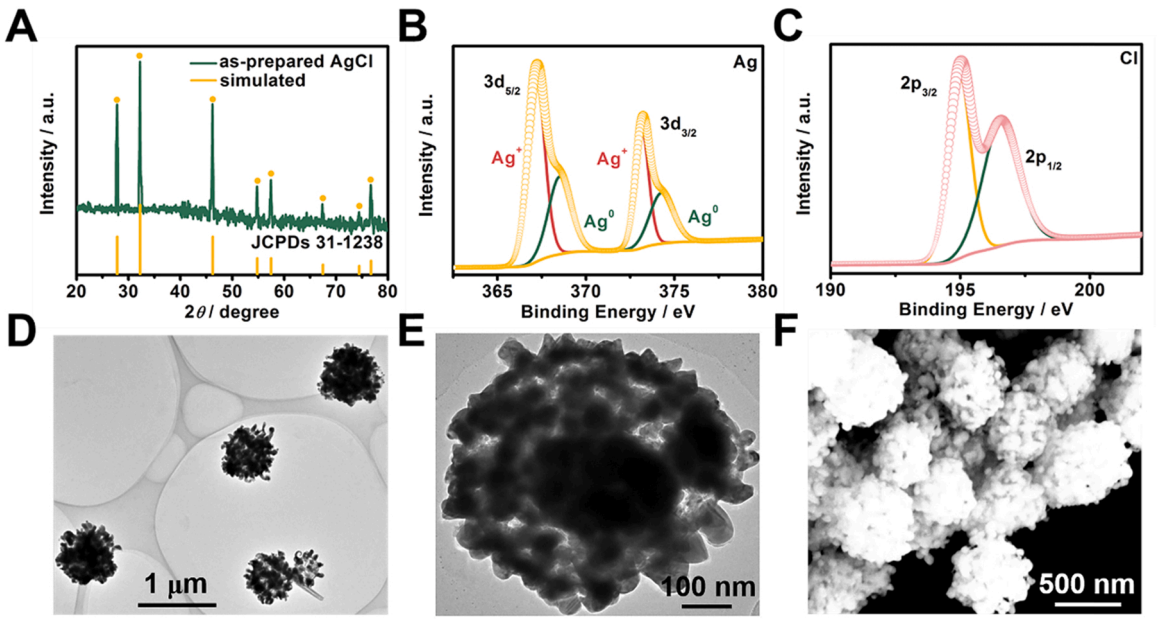

Fig. 2. (A) XRD patterns of as-synthesized AgCl RRNCs and simulated AgCl. XPS spectra in the (B) Ag 3d and (C) Cl 2p regions of AgCl RRNCs. (D-E) TEM images and (F) SEM image of AgCl RRNCs.

at 419.2 and 451.1 nm, which were assigned to $4f^7 \rightarrow 4f^7$ and $4f^6 5d^1 \rightarrow 4f^7$ transition of Eu^{2+} respectively [13,29]. The peaks at 618 and 684 nm belonged to the $^5D_0$-$^7F_2$ and $^5D_0$-$^7F_4$ transitions of Eu^{3+} (Fig. 3B-C) [6]. Given that these results, the luminescence mechanism was regarded as the co-luminescence of Eu^{2+} and Eu^{3+}, and the luminescence of Eu^{3+} was arised from the sensitization of Eu^{2+} (Fig. 3H). Moreover, the antenna effect was testified by testing the excitation spectrum under emission wavelength of 451.1 nm. In Fig. 3D, the excitation peak at 225 nm was assigned to the $\pi - \pi^*$ transitions of the ligand, which demonstrated the energy transfer from ligand to Eu^{2+}. The Fig. 3 G displayed the simple models of the antenna effect and the sensitization based on the density functional theory (DFT) calculations. In the antenna effect, the ligand 1,3,5-benzenetricarboxylic acid and 2-aminoterephthalic acid transferred energy from triplet first excited state (T_1, 21, 509.1 cm^{-1} and 16,372.0 cm^{-1} respectively) to proper $4f^7$ configuration level of Eu^{2+} by nonradiative energy transmission after exciting to their singlet state (S_1) from ground state (S_0) with excitation energy of 26, 052.6 and 24,786.3 cm^{-1} respectively. Subsequently, Eu^{2+} emitted fluorescence and backed to its ground state of $^8S_{7/2}$. In the terms of the fluorescence spectrum, the occurrence of antenna effect were speculated to prior to sensitization in achieving $Sr(HCOO)_2$:Eu^{2+}/Eu^{3+} efficient luminescence by transferring the energy from the $4f^6 5d^1$ level of Eu^{2+} to the $^5D_0$ level of Eu^{3+}.

3.4. The ECL mechanism of the established biosensor

The research of the ECL mechanism of $Sr(HCOO)_2$:Eu^{2+}/Eu^{3+} integrated by CV and ECL spectrum. Firstly, the CV measurements of $Sr(HCOO)_2$:Eu^{2+}/Eu^{3+} in PBS contained 80 mM $K_2S_2O_8$ and in MeCN containing 0.1 M tetra-n-butylammonium perchlorate were carried out. From Fig. 3E, the reduction peak of $Sr(HCOO)_2$:Eu^{2+}/Eu^{3+} was observed at − 1.12 V, the similar reduction peak of $Sr(HCOO)_2$:Eu^{2+}/Eu^{3+} existed in the $K_2S_2O_8$ environment with the new reduction peak of $S_2O_8^{2-} \rightarrow SO_4^{\bullet -}$ at about − 1.72 V, and no oxidation peak was detected in measurements, which indicated that the electrons only injected into the lowest unoccupied molecular orbital (LUMO) of $Sr(HCOO)_2$:Eu^{2+}/Eu^{3+} to form $Sr(HCOO)_2$:Eu^{2+}/$Eu^{3+\bullet -}$ [9], and confirmed the leading ECL center of Eu^{3+}. The ECL enhancement mechanism was verified by the research for catalyzed object of AgCl RRNCs. As can be seen in Fig. 3 F and S6, the ECL signal was improved under the effect of AgCl RRNCs in the $K_2S_2O_8$ environment compared with the biosensor of only $Sr(HCOO)_2$:Eu^{2+}/Eu^{3+}. When tested in pure PBS, the ECL signals were very low, and the biosensor with AgCl RRNCs enhanced faintly compared with the biosensor of only $Sr(HCOO)_2$:Eu^{2+}/Eu^{3+}. These proved the single catalysis of AgCl RRNCs on $K_2S_2O_8$ rather than $Sr(HCOO)_2$:Eu^{2+}/Eu^{3+}. The electron paramagnetic resonance experiment with DMPO as a radical scavenger was used to explore the production of anion sulfate radical $SO_4^{\bullet -}$ from $K_2S_2O_8$ solution after catalysis of AgCl RRNCs. As shown in Fig. S5, when there was no catalyst in the system, the faint free radical peaks of $OH^{\bullet}$ were observed due to the decomposition of H_2O. When AgCl RRNCs was added into the system, obvious DMPO-$OH^{\bullet}$ (the typical 1:2:2:1 peaks) and DMPO-$SO_4^{\bullet -}$ peaks were captured [30], which illustrated that the catalyst can catalyze $K_2S_2O_8$ to generate $OH^{\bullet}$ and $SO_4^{\bullet -}$ simultaneously. Based on these, the ECL mechanism of $Sr(HCOO)_2$:Eu^{2+}/Eu^{3+} leaning on $K_2S_2O_8$ was speculated, and the related ECL mechanism was exhibited in the Fig. 3I and Eq. (1–7) [7,14]:

Path 1.

$$S_2O_8^{2-} + e^- \rightarrow SO_4^{2-} + SO_4^{\bullet -} \quad (1)$$

Path 2.

$$Ag^+ + S_2O_8^{2-} \rightarrow Ag^{2+} + SO_4^{2-} + SO_4^{\bullet -} \text{ (more)} \quad (2)$$

$$SO_4^{\bullet -} + H_2O \rightarrow SO_4^{2-} + OH^{\bullet} + H^+ \quad (3)$$

$$OH^{\bullet} + S_2O_8^{2-} \rightarrow O_2 + HSO_4^- + SO_4^{\bullet -} \text{ (more)} \quad (4)$$

Path 3.

$$Sr(HCOO)_2{:}Eu^{2+}/Eu^{3+} + e^- \rightarrow Sr(HCOO)_2{:}Eu^{2+}/Eu^{3+\,\bullet -} \quad (5)$$

$$Sr(HCOO)_2{:}Eu^{2+}/Eu^{3+\,\bullet -} + SO_4^{\bullet -} \rightarrow Sr(HCOO)_2{:}Eu^{2+}/Eu^{3+*} + SO_4^{2-} \quad (6)$$

$$Sr(HCOO)_2{:}Eu^{2+}/Eu^{3+*} \rightarrow Sr(HCOO)_2{:}Eu^{2+}/Eu^{3+} + h\nu \quad (7)$$

3.5. Application of ECL sensor for CYFRA 21-1 detection

In terms of the ECL property for the proposed immunosensor, utilizing CV and EIS measurements to identify the successful construction of sensor is primary (Fig. S7). Then the working conditions of the ECL

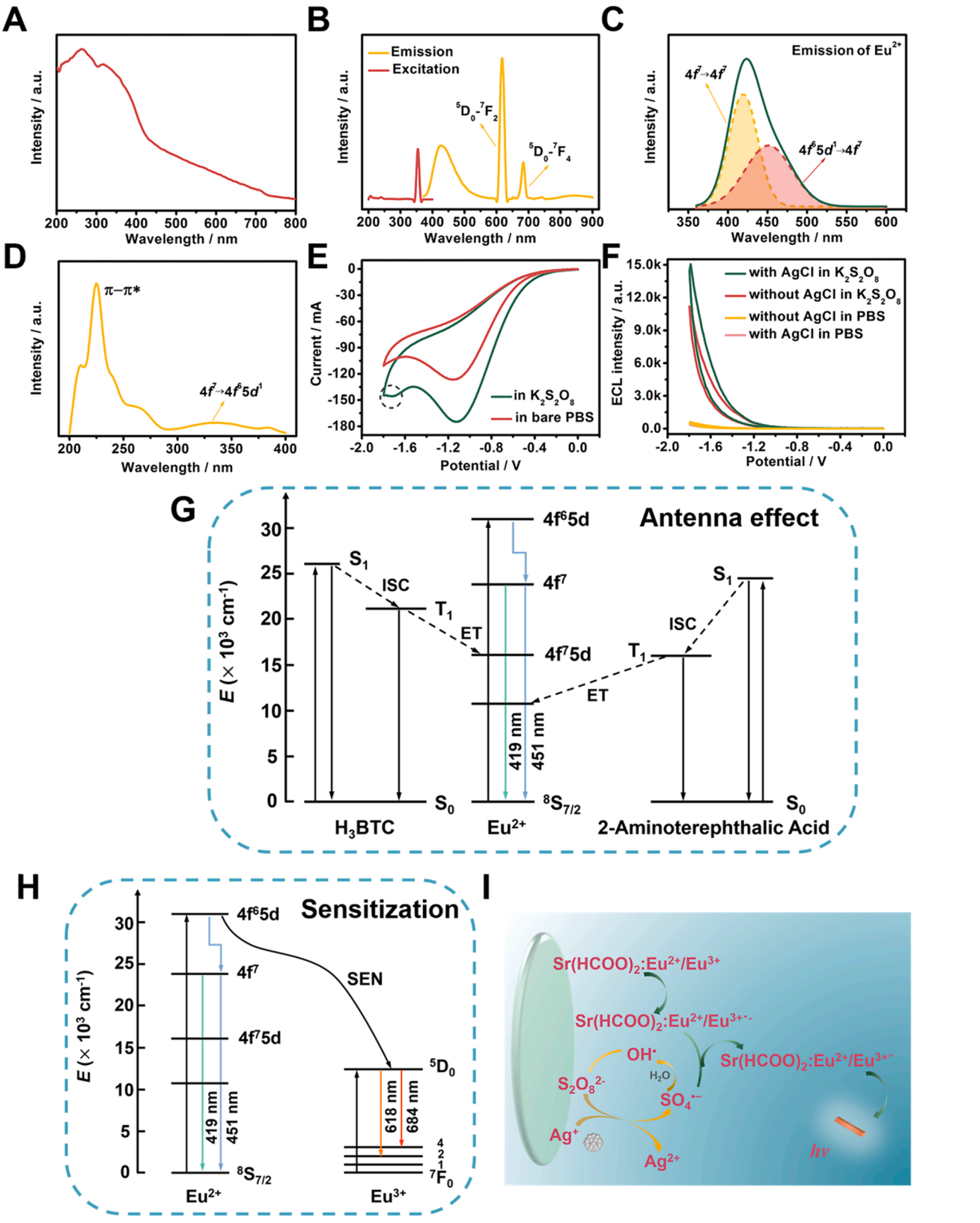

Fig. 3. (A) UV–vis spectrum of $Sr(HCOO)_2$:Eu^{2+}/Eu^{3+}. (B) Fluorescence spectra of $Sr(HCOO)_2$:Eu^{2+}/Eu^{3+}. (C) Fluorescence emission spectra of $4f^7 \rightarrow 4f^7$ and $4f^65d^1 \rightarrow 4f^7$ transition of Eu^{2+} excited at 354 nm. (D) Fluorescence excitation spectrum of $Sr(HCOO)_2$:Eu^{2+}/Eu^{3+} under the emission peak at 451.1 nm of Eu^{2+}. (E) The CV curves of $Sr(HCOO)_2$:Eu^{2+}/Eu^{3+} with and without $K_2S_2O_8$. (F) ECL-potential curves of diverse assembled electrodes with and without AgCl RRNCs in PBS contained $K_2S_2O_8$ or bare PBS. (G-H) Simple models for the antenna effect of ligand to Eu^{2+} and the sensitization of Eu^{2+} to Eu^{3+}. (I) The ECL mechanism of the established biosensor in $K_2S_2O_8$.

sensor need to be optimized, such as pH, the concentrations of coreactant, catalyst and luminophore (Fig. S8). Importantly, the working curves were tested to quantitative detect for CYFRA 21-1. As shown in the Fig. 4A-B, the ECL signals increased regularly as the concentration of CYFRA 21-1 antigen increased from 5 fg/mL to 100 ng/mL with the linear equation of $I = 1502.45 \lg c + 5995.65$ ($R^2 = 0.995$). The acquired LOD was 2.73 fg/mL and lower than the published detection methods for CYFRA 21-1 (Table S1). Furthermore, evaluating the selectivity, reproducibility and stability of the proposed ECL sensor was fundamental for analytical sensing applications. Firstly, the stability was verified under random concentrations between 5 fg/mL~100 ng/mL. From Fig. 4 C, the ECL signals of the proposed biosensor with different CYFRA 21-1 concentrations in a period of test time can keep stabilization, which indicated the good stability of the proposed ECL biosensor. Secondly, fine distinction lied in seven electrodes with uniform sensor, the relative standard deviation (RSD) was 3.0%, indicating the excellent reproducibility of the constructed ECL sensor (Fig. S9). Finally, the acceptable selectivity was embodied in Fig. 4D, in which the low ECL signals were reacted in interferents (1 μg/mL) and strong ECL signals were reacted in CYFRA 21-1 (100 ng/mL) and mixture (CYFRA 21-1 of 100 ng/mL + interferents of 1 μg/mL). To sum up, the proposed ECL biosensor with $Sr(HCOO)_2$:Eu^{2+}/Eu^{3+} and AgCl RRNCs had good ECL performances for efficient detection.

In terms of the practicability for the proposed ECL biosensor, the real samples analysis for human serum is particularly important. We obtained three human serum samples and took the average of the three tests as the initial concentration. Prior to measurement, the samples were centrifugated to obtain the supernatant (9000 rpm, 2 times). Subsequently calculating the recovery rates and RSD values were proceeded after the standard addition method. The suitable recovery rates and RSD values were in the range of 96.7-102% and 1.4–3.5% respectively (Table S2). which verified good accuracy and precision of the established ECL biosensor. Given that the good accuracy and precision, the assembled ECL biosensor met the need of trace detection of CYFRA 21-1 in the clinical diagnosis of non-small-cell lung cancer absolutely.

4. Conclusion

In this work, the efficient ECL biosensor was successfully constructed to ultrasensitive analysis for CYFRA 21-1, in which $Sr(HCOO)_2$:Eu^{2+}/Eu^{3+} with the strong characteristic fluorescence was utilized as luminophore and AgCl RRNCs was used as coreactant accelerator. The Sr $(HCOO)_2$:Eu^{2+}/Eu^{3+} was synthesized by substitutional coordination strategy. By means of UV–vis, fluorescence spectra and DFT calculation, it is proved that the mechanism of $Sr(HCOO)_2$:Eu^{2+}/Eu^{3+} luminescence is first antenna effect of ligand and then sensitization of Eu^{2+}, finally Eu^{2+} and Eu^{3+} luminesced jointly and efficiently. Moreover, the AgCl RRNCs with abundant active sites had good catalytic performance for $S_2O_8^{2-}$, which further enhanced the ECL signals. Thereout, the constructed ECL biosensor presented a wonderful accuracy and precision with low LOD of 2.73 fg/mL and good recovery rate of 96.7–102%. This method will provide a considerable mind to constructed sensor device to realize efficient trace monitoring of non-small-cell lung cancer in clinical diagnose and treatment.

CRediT authorship contribution statement

Lu Zhao: Conceptualization, Data curation, Writing – original draft. **Beibei Wang**: Methodology, Data curation, Review & editing. **Chao Wang**: Methodology. **Dawei Fan**: Formal analysis. **Xuejing Liu**: Methodology, Supervision. **Qin Wei**: Funding acquisition, Formal analysis. **Dan Wu**: Funding acquisition, Project administration, Review & editing. **Huangxian Ju**: Funding acquisition.

Declaration of Competing Interest

The authors declare that they have no known competing financial interests or personal relationships that could have appeared to influence the work reported in this paper.

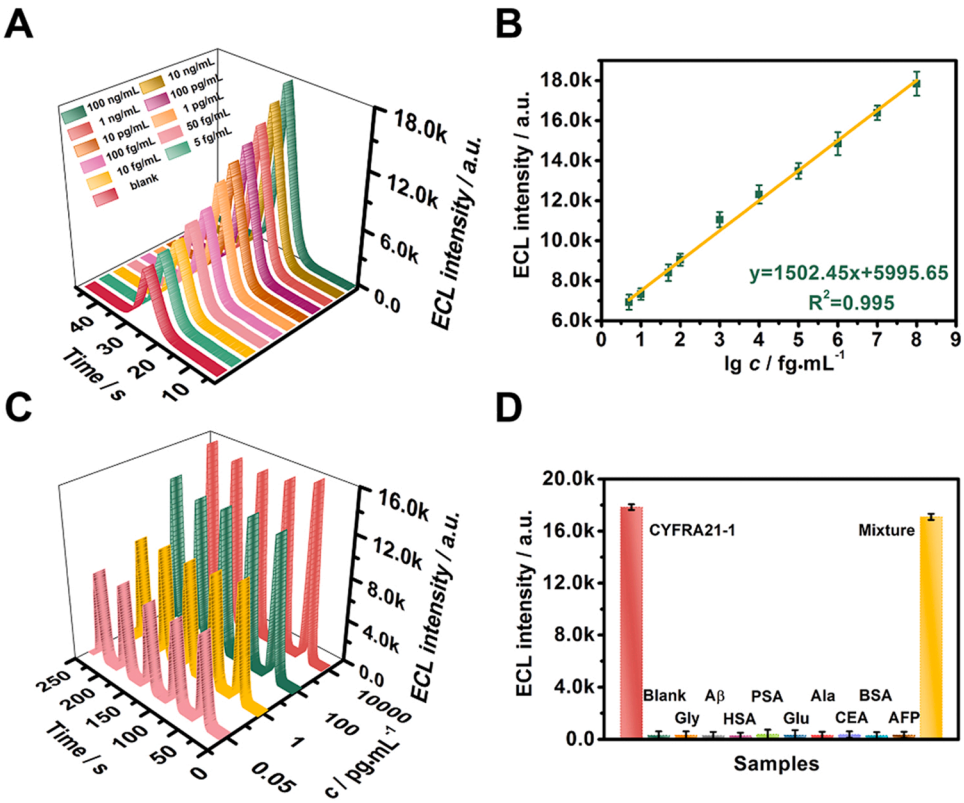

Fig. 4. (A) ECL intensity-time curves and (B) the corresponding linear equation of the constructed ECL biosensor for CYFRA 21-1 detection under a wide concentration range of 5 fg/mL~100 ng/mL. (C) Stability test of the assembled ECL biosensor under different CYFRA 21-1 concentrations in the same test condition. (D) Selectivity tests under various interferences (1 μg/mL) of glycine (Gly), amyloid-β (Aβ), human serum albumin (HSA), prostate-specific antigen (PSA), glucose (Glu), Alanine (Ala), arcinoembryonic antigen (CEA), bovine serum albumin (BSA), alpha-fetoprotein (AFP) and 100 ng/mL of CYFRA21-1. Error bars = SD, ($n = 3$). All experiments were carried out under optimal conditions.

Data availability

Data will be made available on request.

Acknowledgments

This work was supported by the Young Taishan Scholars Program of Shandong Province (tsqn201909124), the Natural Science Foundation of Shandong Province (ZR2021MH037), the China Postdoctoral Science Foundation (2022M711319), the Project of "20 items of University" of Jinan (2019GXRC018), the Innovation Team Project of Colleges and Universities in Jinan (2019GXRC027). All of authors express their sincere thanks.

Supplementary data

Chemicals and apparatus, XPS survey spectrum of as-prepared Sr $(HCOO)_2$:Eu^{2+}/Eu^{3+} and AgCl RRNCs, SEM elemental mapping of Sr, Eu, O and N for Sr$(HCOO)_2$:Eu^{2+}/Eu^{3+} and Ag and Cl for AgCl RRNCs, EPR spectra under AgCl RRNCs catalysis and no catalyst, electrochemical performance of the biosensor, optimization of experimental conditions, repeatability tests of the biosensor, comparison of different methods and biosensors for CYFRA 21–1 detection, standard addition data of purposed ECL sensor for CYFRA 21–1 detection.

Appendix A. Supporting information

Supplementary data associated with this article can be found in the online version at doi:10.1016/j.snb.2022.133101.

References

[1] X.Z. Song, X.R. Shao, L. Dai, D.W. Fan, X. Ren, X. Sun, C.N. Luo, Q. Wei, Triple amplification of 3,4,9,10-perylenetetracarboxylic acid by Co^{2+}-based metal-organic frameworks and silver-cysteine and its potential application for ultrasensitive assay of procalcitonin, ACS Appl. Mater. Interfaces 12 (2020) 9098–9106.

[2] X.Z. Song, X.J. Li, D. Wei, R. Feng, T. Yan, Y.G. Wang, X. Ren, B. Du, H.M. Ma, Q. Wei, CuS as co-reaction accelerator in PTCA-$K_2S_2O_8$ system for enhancing electrochemiluminescence behavior of PTCA and its application in detection of amyloid-beta protein, Biosens. Bioelectron. 126 (2019) 222–229.

[3] X.Z. Song, L. Zhao, C.N. Luo, X. Ren, L. Yang, Q. Wei, Peptide-based biosensor with a luminescent copper-based metal-organic framework as an electrochemiluminescence emitter for trypsin assay, Anal. Chem. 93 (2021) 9704–9710.

[4] X.Z. Song, L. Zhao, C.N. Luo, X. Ren, X.Y. Wang, L. Yang, Q. Wei, Bioactivity-protective electrochemiluminescence sensor using CeO_2/Co_4N heterostructures as highly effective coreaction accelerators for ultrasensitive immunodetection, Sens. Actuators B 355 (2022) 9098–9106.

[5] S.V. Eliseeva, J.C.G. Bunzli, Lanthanide luminescence for functional materials and bio-sciences, Chem. Soc. Rev. 39 (2010) 189–227.

[6] L. Zhao, X.Z. Song, X. Ren, D.W. Fan, Q. Wei, D. Wu, Rare self-luminous mixed-valence Eu-MOF with a self-enhanced characteristic as a near-infrared fluorescent ECL probe for nondestructive immunodetection, Anal. Chem. 93 (2021) 8613–8621.

[7] L. Zhao, X.Z. Song, X. Ren, H. Wang, D.W. Fan, D. Wu, Q. Wei, Ultrasensitive near-infrared electrochemiluminescence biosensor derived from Eu-MOF with antenna effect and high efficiency catalysis of specific CoS_2 hollow triple shelled nanoboxes for procalcitonin, Biosens. Bioelectron. 191 (2021), 113409.

[8] L. Zhao, M. Wang, X.Z. Song, X.J. Liu, H.X. Ju, H.Q. Ai, Q. Wei, D. Wu, Annihilation luminescent Eu-MOF as a near-infrared electrochemiluminescence probe for trace detection of trenbolone, Chem. Eng. J. 434 (2022), 134691.

[9] L. Zhao, X.Z. Song, H. Wang, X.Y. Wang, D. Wu, Q. Wei, H.X. Ju, Eu(II)-MOF as NIR probe for highly efficient instantaneous anodic electroluminescence realized environmental pollutant trace monitoring, Chem. Eng. J. 446 (2022), 136912.

[10] M.M. Jiao, Q.F. Xu, M.L. Liu, C.L. Yang, Y.J. Yu, Efficient green phosphor realized by Ce^{3+}→Tb^{3+} energy transfer in $Li_3Sc_2(PO_4)_3$ for ultraviolet white light-emitting diodes, Phys. Chem. Chem. Phys. 20 (2018) 26995–27002.

[11] J.Y. Li, L.D. Wang, Z.F. Zhao, B.X. Sun, G. Zhan, H.Y. Liu, Z.Q. Bian, Z.W. Liu, Highly efficient and air-stable Eu(II)-containing azacryptates ready for organic light-emitting diodes, Nat. Commun. 11 (2020) 5218–5225.

[12] T.N. Poe, M.J. Beltran-Leiva, C. Celis-Barros, W.L. Nelson, J.M. Sperling, R. E. Baumbach, H. Ramanantoanina, M. Speldrich, T.E. Albrecht-Schoenzart, Understanding the stabilization and tunability of divalent Europium 2.2.2B cryptates, Inorg. Chem. 60 (2021) 7815–7826.

[13] W. Liu, L.J. Liu, Y.L. Wang, L.H. Chen, J.A. McLeod, L.J. Yang, J. Zhao, Z.Y. Liu, D. W. Juan, Z.F. Chai, T.E. Albrecht-Schmitt, G.K. Liu, S.A. Wang, Tuning mixed-valent Eu^{2+}/Eu^{3+} in strontium formate frameworks for multichannel photoluminescence, Chem. Eur. J. 22 (2016) 11170–11175.

[14] G.P. Anipsitakis, D.D. Dionysiou, Radical generation by the interaction of transition metals with common oxidants, Environ. Sci. Technol. 38 (2004) 3705–3712.

[15] X.C. Li, L. Wang, J.H. Shi, N.X. Du, G.H. He, Multishelled nickel-cobalt oxide hollow microspheres with optimized compositions and shell porosity for high-performance pseudocapacitors, ACS Appl. Mater. Interfaces 8 (2016) 17276–17283.

[16] X.D. Zhang, Y.W. Lu, Q.M. Chen, Y.M. Huang, A tunable bifunctional hollow Co_3O_4/MO_3(M = Mo, W) mixed-metal oxide nanozyme for sensing H_2O_2 and screening acetylcholinesterase activity and its inhibitor, J. Mater. Chem. B 8 (2020) 6459–6468.

[17] Y.G. Feng, J.W. He, D.N. Chen, L.Y. Jiang, A.J. Wang, N. Bao, J.J. Feng, A sandwich-type electrochemical immunosensor for CYFRA 21-1 based on probe-confined in PtPd/polydopamine/hollow carbon spheres coupled with dendritic Au@Rh nanocrystals, Microchim. Acta 189 (2022) 271.

[18] Y.G. Wang, G.H. Zhao, H. Chi, S.H. Yang, Q.F. Niu, D. Wu, W. Cao, T.D. Li, H. M. Ma, Q. Wei, Self-luminescent lanthanide metal-organic frameworks as signal probes in electrochemiluminescence immunoassay, J. Am. Chem. Soc. 143 (2021) 504–512.

[19] N. Lu, A.R. Gao, P.F. Dai, H.J. Mao, X.L. Zuo, C.H. Fan, Y.L. Wang, T. Li, Ultrasensitive detection of dual cancer biomarkers with integrated CMOS-compatible nanowire arrays, Anal. Chem. 87 (2015) 11203–11208.

[20] C.H. An, S. Peng, Y.G. Sun, Facile synthesis of sunlight-driven AgCl:Ag plasmonic nanophotocatalyst, Adv. Mater. 22 (2010) 2570–2574.

[21] S.H. Han, H.M. Liu, C.C. Sun, P.J. Jin, Y. Chen, Photocatalytic performance of AgCl@Ag core-shell nanocubes for the hexavalent chromium reduction, J. Mater. Sci. 53 (2018) 12030–12039.

[22] M.E. Aguirre, R. Isla Naveira, P.M. Botta, T.A. Altieri, A. Wolosiuk, M.S. Churio, Early instability of MIL-125-NH_2 in aqueous solution and mediation of the visible photogeneration of an NADH cofactor, New J. Chem. 45 (2021) 10277–10286.

[23] R.Q. Miao, Q.Q. Zhou, S.Q. Wang, X.Y. Cheng, D.F. Wang, R.B. Huang, Solvent-induced Zn(II) coordination polymers with 1, 3, 5-benzenetricarboxylic acid, J. Mol. Struct. 1184 (2019) 219–224.

[24] H.Y. Li, Y.B. Chen, J.C. Ge, X.H. Liu, A.C. Fisher, M.P. Sherburne, J.W. Ager, Z. J. Xu, Active phase on $SrCo_{1-x}Fe_xO_{3-\delta}$ ($0 \leq x \leq 0.5$) perovskite for water oxidation: reconstructed surface versus remaining bulk, JACS Au 1 (2021) 108–115.

[25] S. Komai, M. Hirano, N. Ohtsu, Spectral analysis of Sr 3d XPS spectrum in Sr-containing hydroxyapatite, Surf. Interface Anal. 52 (2020) 823–828.

[26] D.A. Pawlak, M. Ito, M. Oku, K. Shimamura, T. Fukuda, Interpretation of XPS O (1s) in mixed oxides proved on mixed perovskite crystals, J. Phys. Chem. B 106 (2002) 504–507.

[27] H.Y. Li, T.S. Wu, B. Cai, W.G. Ma, Y.J. Sun, S.Y. Gan, D.X. Han, L. Niu, Efficiently photocatalytic reduction of carcinogenic contaminant Cr (VI) upon robust AgCl:Ag hollow nanocrystals, Appl. Catal. B 164 (2015) 344–351.

[28] M. Van de Voorde, B. Geboes, T. Vander Hoogerstraete, K. Van Hecke, T. Cardinaels, K. Binnemans, Stability of europium(ii) in aqueous nitrate solutions, Dalton Trans. 48 (2019) 14758–14768.

[29] Y. Zhang, X.J. Li, K. Li, H.Z. Lian, M.M. Shang, J. Lin, Crystal-site engineering control for the reduction of Eu^{3+} to Eu^{2+} in $CaYAlO_4$: structure refinement and tunable emission properties, ACS Appl. Mater. Interfaces 7 (2015) 2715–2725.

[30] Z.S. Wei, F.A. Villamena, L.K. Weavers, Kinetics and mechanism of ultrasonic activation of persulfate: an in situ EPR spin trapping study, Environ. Sci. Technol. 51 (2017) 3410–3417.